

A Novel Magnetic Actuation System for Miniature Swimming Robots

Pietro Valdastri, *Member, IEEE*, Edoardo Sinibaldi, Sebastiano Caccavaro, Giuseppe Tortora, *Student Member, IEEE*, Arianna Menciassi, *Member, IEEE*, and Paolo Dario, *Fellow, IEEE*

Abstract—A novel mechanism for actuating a miniature swimming robot is described, modeled, and experimentally validated. Underwater propulsion is obtained through the interaction of mobile internal permanent magnets that move a number of polymeric flaps arranged around the body of the robot. Due to the flexibility of the proposed swimming mechanism, a different range of performances can be obtained by varying the design features. A simple multiphysics dynamic model was developed in order to predict basic behavior in fluids for different structural parameters of the robot. In order to experimentally verify the proposed mechanism and to validate the model, a prototype of the swimming robot was fabricated. The device is 35 mm in length and 18 mm in width and thickness, and the forward motion is provided by four flaps with an active length of 20 mm. The model was able to correctly predict flap dynamics, thrust, and energy expenditure for magnetic dragging within a spindle-frequency range going from 2 to 5 Hz. Additionally, the model was used to infer robot-thrust variation related to different spindle frequencies and a 25% increase in flap active length. Concerning swimming performance, the proposed technical implementation of the concept was able to achieve 37 mm/s with 4.9% magnetic mechanism efficiency.

Index Terms—Elastic magnetic modeling, magnetic actuation, miniature robot, swimming robot.

I. INTRODUCTION

THE continuous quest for miniaturization, which is mainly driven by the evolution of microfabrication and microsystems technologies, has fostered the full development of miniature robots. A miniature robot usually falls in the dimensional range from a few centimeters down to the millimeter scale. Most examples incorporate a control core, a power source, propulsion and steering actuators, and sensors designed for the specific application. Many solutions have been proposed for the development of miniature robots provided with flying, crawling, or

swimming locomotion abilities. Typical applications for these devices range from monitoring complex environments [1] to medical applications [2], [3].

In this study, we address the fascinating and challenging topic of propulsion in fluids, where simple actuators and low forces can be used to achieve effective locomotion, as happens in many small animals [4]. Due to physical scaling laws, miniature robots capable of swimming in fluids cannot be obtained by simply shrinking traditional robots but must be based on radically different and novel concepts [5].

However, due to the small Reynolds numbers at low scales (i.e., in the millimeter range), traditional principles of locomotion, such as fins or propellers, cannot be straightforwardly applied to swimming robots without proper modeling. Since natural microorganisms have evolved in these conditions, biomimetic approaches hold the promise to achieve good and highly efficient performance. An example of swimming robot where the propulsion concept is inspired by flagellar locomotion of bacteria was discussed and modeled in [6]. In [7], the swimming action relies on the creation of a traveling wave along a piezoelectric-layered beam divided into several segments.

By increasing the size up to the centimeter scale, biomimetics still represents a valid approach [8]–[11], even if traditional propulsion mechanisms can also be effectively applied [12].

Developing an actuation concept that can be tailored to a specific application by simply trimming various structural parameters would extend the application of miniature robotics to new scenarios. To achieve this goal, a usable model for the proposed mechanism must be available at the time of robot design [13]–[16]. Such a model would also allow prediction of the swimming performance as the overall dimensions scale down.

In this study, we propose a novel magnetic actuation concept embedded in a miniature swimming robot and inspired by the periodic movement of the jellyfish bell. The robot is based on a rotary actuator, a magnetic rotor, a number of polymeric flaps endowed with magnets, and a plastic body, integrating a wireless microcontroller and power supply. Several design and structural parameters can be varied to tune the swimming performance toward the desired application. To move a first step in this direction, we developed a dynamical model accounting for flap dynamics, thrust, and energy consumption within the operational frequency range of the proposed actuation concept. Being a preliminary and simple model, it is not able to predict robot swimming speed, as will be better detailed in this paper.

Rather than addressing a specific application, the proposed actuation solution can be straightforwardly extended to cope with complex technical problems, thus broadening its impact.

Manuscript received October 27, 2010; revised February 11, 2011; accepted March 16, 2011. Date of publication May 5, 2011; date of current version August 10, 2011. This paper was recommended for publication by Associate Editor K. Kyriakopoulos and Editor B. J. Nelson upon evaluation of the reviewers' comments. This paper was presented in part at the IEEE International Conference on Robotics and Automation, Anchorage, AK, 2010.

P. Valdastri, S. Caccavaro, G. Tortora, A. Menciassi, and P. Dario are with the BioRobotics Institute, Scuola Superiore Sant'Anna, 56127 Pisa, Italy (e-mail: pietro@sssup.it; s.caccavaro@sssup.it; g.tortora@sssup.it; arianna@sssup.it; dario@sssup.it).

E. Sinibaldi is with the Center for Micro-BioRobotics@SSSA, Istituto Italiano di Tecnologia, 56025 Pontedera, Italy (e-mail: edoardo.sinibaldi@iit.it).

This paper has supplementary downloadable material available at <http://ieeexplore.ieee.org> provided by the author. The material includes a movie of the robot. The size of the movie is 9.05 MB. Contact pietro@sssup.it for further questions about this work.

Color versions of one or more of the figures in this paper are available online at <http://ieeexplore.ieee.org>.

Digital Object Identifier 10.1109/TRO.2011.2132910

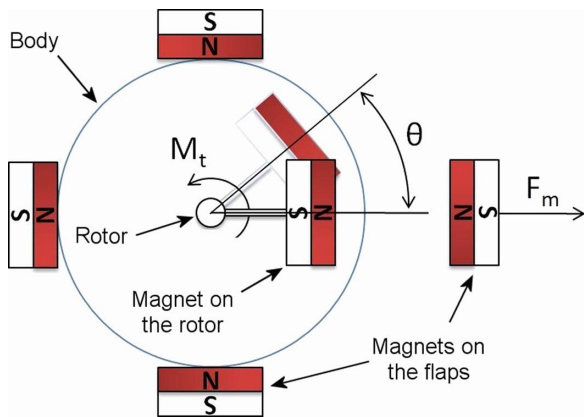


Fig. 1. Schematic representation of the working principle for a repulsive configuration for a single rotating magnet and four flaps.

The discussion presented here serves as a basis for tailored applications. Indeed, a modular approach to miniature-robot design is primarily pursued, which can be extended to other fields, including terrestrial applications. Optimizing performances, e.g., locomotion speed, will be addressed, therefore, at a subsequent stage.

II. WORKING PRINCIPLE

The proposed actuation mechanism relies on the magnetic interaction among permanent magnets. The concept is based on a rotating actuator moving a set of permanent magnets inside the robot body. These magnets interact with polymeric flaps endowed with magnets and hinged to the robot body, thus making them flap.

To a certain extent, this locomotion strategy is reminiscent of jellyfish locomotion should all the flaps be laterally connected together to form an umbrella and contract at the same time. This would allow an axisymmetric motion to be achieved and avoid more complex translational and rotational dynamics.

To better understand the working principle, a configuration may be considered where the motor inside the robot body rotates a support holding a permanent magnet. This permanent magnet, while rotating, sequentially faces the permanent magnets embedded in the flaps. If the magnets are oriented, as shown in Fig. 1, a repulsive force F_m is generated on the external magnet, thereby causing the flap to move outward. If the flap is made out of an elastic material, the elastic force will bring the flap back to the initial position once the internal magnet has rotated away.

Several design and structural parameters can be varied in order to tailor the swimming performance to the desired scenario. In particular, the following are the most-relevant features.

- 1) *Flap design*: A first parameter is the number of flaps, which ranges from a single umbrella as in jellyfishes, to a discrete number of flapping appendices. The flaps can be designed as beams, which are hinged on one end to the robot body with the magnet embedded into the other end, or they can be fixed to the robot body on both sides, with the magnet embedded in between. This latter configura-

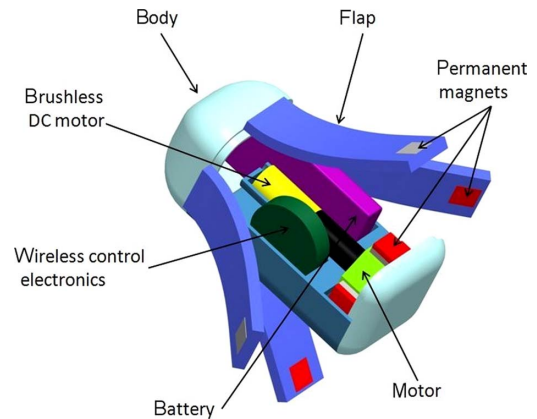


Fig. 2. Three-dimensional sketch of the swimming robot and its internal components.

tion may enable terrestrial locomotion in miniature robotic systems, as given in [17]. The shape of each flap influences the thrust force, while the material determines the flap's mechanical behavior, especially its bending under magnetic force driving. The use of composite materials may be considered as well, with magnetic particles embedded in proximity of the internal rotating magnets.

- 2) *Magnetic link*: The number of internal magnets and their position on the rotor are two important design parameters. If the number of internal magnets is equal to the number of flaps and if they are placed symmetrically on the rotor, a synchronized actuation of the flaps would occur. A tradeoff in the interaction between the internal and external magnets is crucial to obtain the largest flap stroke within the torque range of the actuator. Depending on the relative arrangement of the two sets of magnets, the system can operate either in a repulsive, as shown in Fig. 1, or in an attractive configuration. Hybrid arrangements are also possible, depending on the desired behavior.
- 3) *Actuator*: The actuator is responsible for providing the torque M_t to rotate the internal magnets. A rotational actuator, such as a dc motor, may be chosen. However, a traditional actuator would prevent the robot from scaling down to the millimeter scale. For this size range, piezoelectric motors or microelectromechanical systems actuators should be considered. Rotational speed, as better detailed afterward, is a crucial parameter that can be optimized through modeling.
- 4) *Robot body*: The robot shell must be waterproof and large enough to accommodate all the internal components. A smooth-body design, having a low drag coefficient in fluids, may enhance swimming performance.

A schematic representation of a robot implementing the proposed swimming principle is represented in Fig. 2. A symmetrical swimming motion is obtained by providing the device with a rotor incorporating four permanent magnets, and four flaps, with each embedding a permanent magnet at the level of the rotor, which are arranged in the repulsive configuration. A battery-operated brushless dc motor rotates the internal magnets, thus

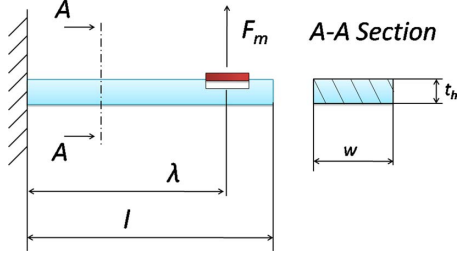


Fig. 3. (Lateral view) Schematic of the flap, which is described as a clamped beam, which shows relevant geometrical parameters as well. The on-flap magnet is also shown, which is subjected to the magnetic force F_m .

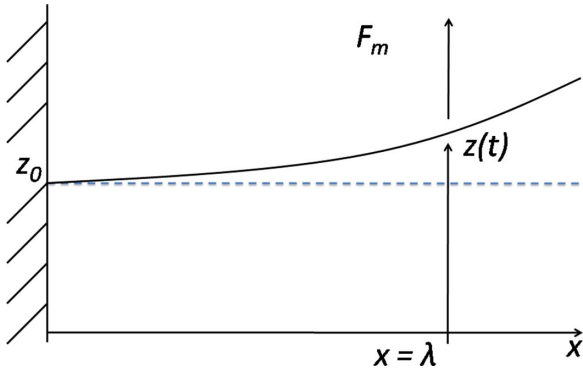


Fig. 4. Schematic of the beam midline deflection due to a static load F_m . Both the (dashed line) undeformed and the (solid line) deformed configuration are shown.

adjusting rotational speed upon user request due to wireless control electronics.

III. MODELING

In the following section, a dynamical model of the working principle introduced in Section II is reported.

A. Model Definition

1) *Simplified Beam Dynamics*: From Fig. 2, a single flap is considered by symmetry, having an active length l and a rectangular cross-section with thickness t_h and width w . A beam approximation is introduced for the flap at hand, despite the fact that the w/l ratio might not necessarily be small (e.g., 0.5 in the proposed robot implementation). This approximation, like others further introduced, is regarded as a working assumption to be assessed during the validation phase. A lateral sketch of the flap is reported in Fig. 3. The on-flap magnet is also shown, which is placed at a distance λ from the flap-clamped section and subjected to the magnetic force F_m .

Let us now consider the beam static deflection, as caused by a constant load F_m . With reference to Fig. 4, an abscissa x is first introduced so that the load is applied at $x = \lambda$. Moreover, let z denote the deflection of the beam midplane at $x = \lambda$, and let $\xi = x/\lambda$ represent a nondimensional abscissa. Then, by recalling classical results from the linear beam theory [18], the

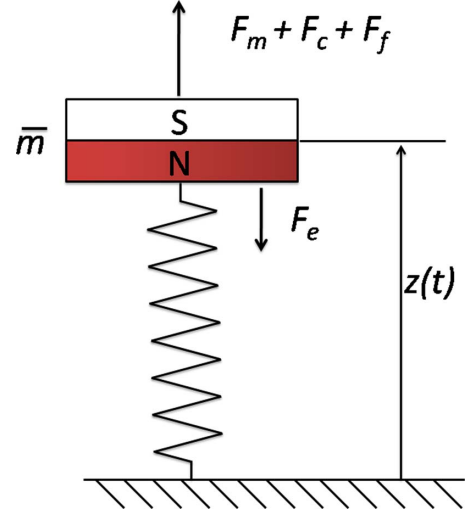


Fig. 5. Schematic of the simplified, 1-D system indicating relevant forces as well.

deformed shape for $0 \leq x \leq \lambda$ reads

$$\frac{\zeta}{z} = \frac{1}{2} (3 - \xi) \xi^2 \quad (1)$$

where $\zeta = \zeta(\xi)$ denotes the displacement at the generic abscissa $x = \lambda \xi$. In addition, for $\lambda < x \leq l$, the deformed shape is straight, with the slope of the cubic-shape function (1) at $\xi = 1$. A characteristic time for beam perturbations can be estimated as $\tau_p = l/c$, where $c = \sqrt{E/\rho}$ denotes the beam sound speed, and E and ρ denote the Young's modulus and density, respectively. Considering the periodic mechanism driving the proposed actuation system, τ_p must be compared with the time interval τ_m occurring between the passage of two subsequent rotating magnets underneath the beam, namely, $\tau_m = 1/(N_m f)$, where f denotes the rotation frequency, and N_m denotes the number of magnets on the rotor. By assuming $N_m = 4$ magnets rotating at $f = 4$ Hz, we get $\tau_m \approx 6.25 \times 10^{-2}$ s. On the other hand, by considering an $l = 20$ -mm-long flap made with the material specified in Section IV, we get $\tau_p \approx 4.84 \times 10^{-4}$ s. Hence, being $\tau_p \ll \tau_m$, it is reasonable to assume that the flap shape at the generic time t be determined by the beam deflection $z = z(t)$ via the shape function (1). This assumption still holds when deriving τ_p from the first-mode natural frequency of the flap, which is treated as a clamped beam [18]. Due to this approximation, the 2-D dynamics is reduced to a simplified, 1-D lumped-parameters model. This approximation is also commonly adopted when studying cantilever dynamics for a variety of applications, including, e.g., scanning force microscopy and energy harvesting [19]. In particular, an equivalent mass \bar{m} is introduced for defining the $z(t)$ dynamics, derived from energy considerations. For a rectangular cross-section beam, $\bar{m} \approx m_m + (33/140) m_b$, where m_m and m_b , respectively, denote the mass of the magnet and of the beam.

A schematic representation of the 1-D system is shown in Fig. 5.

In consideration of the previous points, the simplified 1-D dynamics reads

$$\begin{cases} \bar{m} \ddot{z} = F_m(z) - F_e(z) + F_f(\dot{z}) + F_c(z, \dot{z}) \\ z(t=0) = z_0 \end{cases} \quad (2)$$

where F_m , F_e , F_f , and F_c , respectively, represent the magnetic force, the elastic force, the fluidic force, and the contact force (the latter only playing a role when the flap impacts on the body wall). It is worth highlighting that (2) is the main dynamic model in this paper and its result will later be used for computing the robot thrust force. Relevant force submodels are introduced below. In general, the right-hand-side terms in (2) lead to a nonlinear ordinary differential equation, which can only be solved by numerical integration. An explicit Runge–Kutta schema (fourth–fifth-order accurate as per the Dormand–Prince variant) has been considered in this study [20].

2) *Magnetic Driving Force*: N_m identical, parallelepiped, rotating magnets are considered, in addition to the one fixed on the flap. For details, see Section IV. Moreover, the N_m magnets are assumed to rotate within the plane $x = \lambda$, with known angular velocity $\omega = 2\pi f$. Hence, once we define the center of rotation \vec{C}_m as well as the radial distance between the center of each parallelepiped and \vec{C}_m , the magnet's configuration is completely defined. In particular, the position $\vec{P}_{m,k}$ of the k th magnet is defined as well as the corresponding radial unit vector $\hat{e}_{r,k} = (\vec{P}_{m,k} - \vec{C}_m) / \|\vec{P}_{m,k} - \vec{C}_m\|$.

A dipole approximation is then adopted for each magnet: a dipole moment $\vec{m}_k = \bar{m} \hat{e}_{r,k}$ is associated with the k th magnet, for $k = 1, \dots, N_m$ (parameter \bar{m} represents the dipole intensity and is given a value through calibration; see Section III-B). Moreover, a dipole moment $\vec{m}_0 = -\bar{m} \hat{e}_z$ is associated with the flapping magnet, where \hat{e}_z denotes the z -axis unit vector.

At the generic time t , the flapping-magnet position is given by $\vec{P} = \vec{P}(t) = (\lambda, 0, z(t))$ (the $y = 0$ coordinate is by symmetry: indeed, the $y = 0$ plane is the one represented in Figs. 3 and 4). Then, the magnetic field produced by the k th rotating magnet at point \vec{P} reads [21]

$$\vec{B}_k = \frac{\mu_0}{4\pi} \left[\frac{3(\vec{m}_k \cdot \hat{r}_k) \hat{r}_k}{r_k^3} - \frac{\vec{m}_k}{r_k^3} \right] \quad (3)$$

where $\vec{r}_k = \vec{P} - \vec{P}_{m,k}$, $r_k = \|\vec{r}_k\|$, $\hat{r}_k = \vec{r}_k/r_k$, and μ_0 denotes the vacuum magnetic permeability. The corresponding force acting on the flapping magnet is given by [21]

$$\begin{aligned} \vec{F}_k = & \frac{3\mu_0}{4\pi r_k^5} \left[(\vec{m}_k \cdot \vec{r}_k) \vec{m}_0 + (\vec{m}_0 \cdot \vec{r}_k) \vec{m}_k \right. \\ & \left. + (\vec{m}_k \cdot \vec{m}_0) \vec{r}_k - \frac{5(\vec{m}_k \cdot \vec{r}_k)(\vec{m}_0 \cdot \vec{r}_k)}{r_k^2} \vec{r}_k \right] \end{aligned}$$

from which the relevant magnetic force is directly obtained by superposition and projection along the z -axis, namely

$$F_m = \left(\sum_{k=1}^{N_m} \vec{F}_k \right) \cdot \hat{e}_z. \quad (4)$$

3) *Elastic Force*: Consistently with the linear result (1), a linear spring is introduced for modeling the beam elastic force, namely

$$F_e(z) = k_b (z - z_0) \quad (5)$$

where the stiffness constant k_b is directly derived from beam theory as follows:

$$k_b = \frac{3EI}{\lambda^3} \quad (6)$$

with $I = w t_h^3/12$ representing the relevant cross-sectional inertia moment.

4) *Fluidic Force*: In order to estimate a Reynolds number for the flapping beam, a characteristic length $l_{\text{ref}} \approx 10^{-2}$ m is chosen (see Section IV for flap size). Then, a reference speed is estimated by assuming the flapping spans a distance $s_{\text{ref}} \approx 5 \times 10^{-3}$ m during a reference time $t_{\text{ref}} = \tau_m/2 \approx 3 \times 10^{-2}$ s. With this choice, we estimate a characteristic Reynolds number as $Re = (l_{\text{ref}} s_{\text{ref}}) / (\nu t_{\text{ref}}) \approx 2 \times 10^3$, having chosen the water kinematic viscosity $\nu \approx 10^{-6}$ m²/s. Such a value is high enough not to justify the exploitation of a simplified, linear damping model for fluidic actions. On the other hand, it is not high enough to assume a fully developed turbulent flow, thus providing hints on the complexity of the unsteady-flow regime arising during flapping. In this spirit, an empirical model is introduced, which is defined as follows:

$$F_f = -C_d (\rho_f l w) |\dot{z}| \dot{z} \quad (7)$$

where C_d is an empirical positive parameter (as defined by calibration later in this paper), ρ_f is the fluid density accounting for fluid inertial effects, and lw is the flap top surface, which is commonly adopted for fluidic force scaling.

5) *Wall Contact Force*: Contact with the case wall occurs during ordinary flapping regimes. Since the fluid considerably mediates the contact at hand, no flap rebounds take place, in practice, and it is possible to describe this effect through a nonlinear damping model. In particular, the following expression is adopted:

$$F_c = -\chi(z, \dot{z}) C_c \dot{z} \quad (8)$$

where χ is a step-like function, being defined as

$$\chi(z, \dot{z}) = \begin{cases} 1, & \text{if } \dot{z} < 0 \text{ and } |z - z_0| < \delta_c \\ 0, & \text{otherwise} \end{cases}$$

where C_c is a numerical positive damping coefficient, and δ_c is a positive numerical threshold for contact detection. They are given a suitable value to keep the wall-contact effect as confined as possible, consistently with observation.

6) *Free Model Parameters—A Remark*: Besides geometrical parameters (which are fixed in the design phase), only two parameters need to be assigned in order to integrate the dynamical model (2): the magnetic dipole moment \bar{m} and the fluidic damping coefficient C_d . Both are defined below by calibration. After calibration, the model is, in principle, ready for predictions. As anticipated, the numerical parameters involved in the contact model are fixed so as to obtain a local effect during flap–wall

contact, consistently with observation. In particular, δ_c is chosen to be “small” with respect to the beam thickness t_h , while C_c is empirically chosen so as to prevent beam-wall penetration, yet minimizing energy dissipation in order to not fictitiously alter the flap dynamics (i.e., the value of C_c is increased until the no-penetration condition is obtained).

7) *Robot Thrust*: The average robot thrust due to flapping (i.e., the force propelling the robot along the x -axis sketched in Fig. 4, in the negative x -direction) is estimated by recalling relevant results from the large-amplitude elongated-body theory originally developed by Lighthill to study fish locomotion [22]. Particularly, regarding the flap as a swimming body with periodically changing shape, it is possible to estimate the average thrust per period F_x^{prop} by

$$F_x^{\text{prop}} = -m_v \left\langle v_{T,n} \dot{\zeta}_T + \frac{1}{2} v_{T,n}^2 \cos(\theta_T) \right\rangle \quad (9)$$

where v_n is the normal-velocity component, θ is defined by $\tan(\theta) = d\zeta/dx$, subscript T indicates that relevant entities are picked at the beam tip, and $\langle \cdot \rangle$ denotes time averaging over the flapping period. Moreover, m_v is a “virtual mass” per unit length coefficient. For a rigid body moving within a fluid with speed \bar{u} , the virtual mass M_v is defined so that $M_v \bar{u}^2/2$ is equal to the kinetic energy of the entire fluid field. For a deformable body, this definition is more involved (indeed, there are some open issues in this regard [22]). However, an estimate for the flapping device at hand could be derived as $m_v \approx \rho_f w t_v$, where ρ_f stands for the fluid density, and t_v denotes a “virtual thickness” of the flap. It seems reasonable to assume t_v in the range $[t_h, d_{cs}]$, where d_{cs} indicates a characteristic diameter of the robot cross section. In order to obtain an estimate of the flapping thrust by (9), we assume $t_v \approx (t_h + d_{cs})/2$. The elongated-body theory is chosen for its relative simplicity, since it can be combined with the proposed, simplified dynamical model with minor efforts. More complex modeling techniques have been developed for thrust formation by flapping bodies [23], thereby addressing basic phenomena such as flow over the edge, vortex formation and shedding, delayed separation, and stall. However, such an accuracy level in fluidic modeling is beyond the scope of this study, and it will be tackled in future studies, dealing with more specific robotic implementations.

8) *Magnetic Torque*: A constant angular speed is assumed for the rotating magnets, i.e., their dynamics is imposed as input to the model. However, magnetic forces acting between the flapping magnets and the rotating ones tend to slow down the spindle rotation. The magnetic torque \vec{T}_m can be straightforwardly estimated by the proposed model as follows:

$$\vec{T}_m = - \sum_{k=1}^{N_m} \left(\vec{P}_{m,k} - \vec{C}_m \right) \times \vec{F}_{m,k} \quad (10)$$

where $\vec{F}_{m,k}$ is the magnetic force due to the k th rotating magnet on the flapping one. Then, the magnetic resistant (MR) torque T_m^{res} is directly obtained as the x -component of (10).

B. Model Parameters: Calibration and Assessment

1) *Magnetic Dipole Intensity*: Let us consider the magnetic dipole intensity introduced above. In order to give \tilde{m} a value, two facing magnets are considered, which are oriented in order to generate a repulsive force F_m^{rep} on each other as a function of the distance δ_m separating their centers. According to the considered dipole approximation [21], the intensity of the repulsive force is given by the following expression:

$$|F_m^{\text{rep}}(\delta_m)| = \frac{\mu_0}{4\pi} \frac{6\tilde{m}^2}{\delta_m^4}. \quad (11)$$

Experimental data for $|F_m^{\text{rep}}(\delta_m)|$ are available from the manufacturer of the chosen magnets (see Section IV). By fitting the considered data to (11), \tilde{m} was estimated as $9.11 \times 10^{-3} \text{ A} \cdot \text{m}^2$. The fitting was performed for $\delta_m \geq \delta_*$, where δ_* is a lower threshold defined by envisaged geometrical constraints (see Section IV).

2) *Beam Stiffness*: Before considering beam dynamical behavior, the suitability of the estimate (6) of beam stiffness was assessed. The static deflection of the flap, which was caused by the repulsive force of facing magnets, was measured by processing images taken from the experimental setup. Then, numerical simulations have been carried out by considering nonrotating magnets, up to a regime state defining the static, deformed configuration that is unaffected by fluidic damping. It was assessed that the adopted expression (6), which is to be substituted into (5), indeed predicts flap deflection, thus underestimating the experimentally observed value by just 4%. Underestimation is due to the perfect clamping assumed within the model.

3) *Fluidic Damping Coefficient*: Once the calibration and assessment steps above were performed, the coefficient C_d in (7) was given a value by measuring the amplitude of the regime oscillations of a given flap, immersed in water and actuated at known working condition. At a first stage, a single flap—yet representative of the currently envisaged system—was deliberately considered for calibration (thus avoiding, e.g., best-fit procedures) to assess the model’s predictive capabilities based on a few empirical data. The resulting value was $C_d \approx 0.3$; this is the only model parameter defined using an essentially empirical approach.

C. Model Output

The main model outputs are discussed below. Additional entities to be predicted by the proposed model can be easily introduced by virtue of the adopted modular approach.

1) *Flap Dynamics*: Flap (i.e., beam) dynamics, especially beam displacement $\zeta(x, t)$, represents the primary output of the proposed computational model. For instance, Fig. 6 shows beam displacement at $x = \lambda$ [i.e., the function $z(t)$ obtained by integrating (2)] over a flapping period.

In the same figure, relevant forces—of a magnetic, elastic, fluidic, and contact nature—are also shown, over the same time interval. By comparatively observing the flap displacement and the forces involved, it is possible to understand the role and the relative importance of the latter in determining flap dynamics. This allows for a deep understanding of the key design

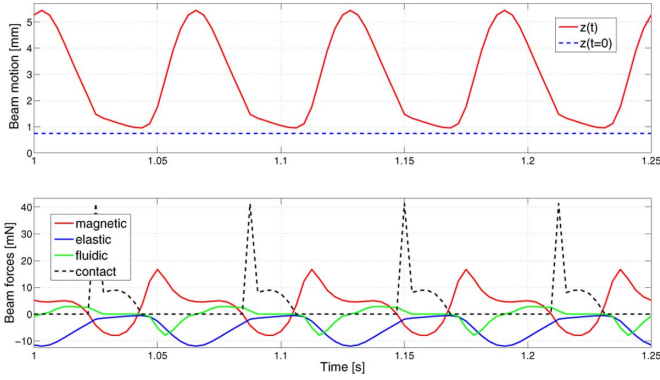


Fig. 6. Example of beam (i.e., flap) (top) displacement $z(t)$ over a period, with (bottom) corresponding forces F_m (i.e., magnetic), F_e (i.e., elastic), F_f (i.e., fluidic), and F_c (i.e., contact). Flap size: $20 \times 10 \times 1.5$ mm ($l \times w \times t_h$). Young's modulus 1.76×10^6 N/m². Magnets data, as reported in Section IV; rotation frequency $f = 4$ Hz.

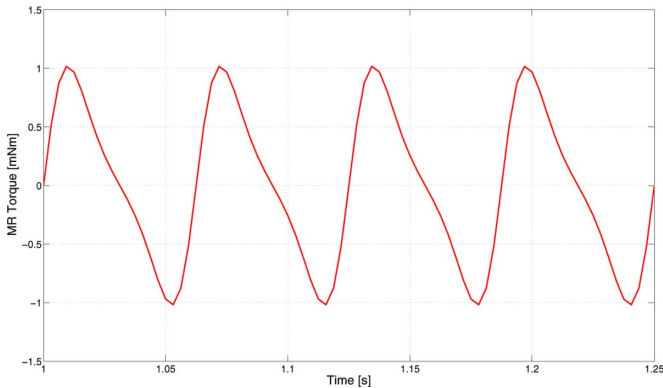


Fig. 7. Trend of the MR torque, as obtained by forcing the flapping magnet not to move. Parameters are as reported in Fig. 6.

principles to be adopted when targeting a specific flap behavior. Moreover, it is possible to investigate the effect a chosen design parameter has on flap dynamics. For example, as suggested by physical intuition (see Section V as well), the number of wall-flap contacts during a period decreases when the frequency f of the rotating magnets is raised above a certain value. Within the proposed modeling framework, such an effect would be directly revealed through a null-contact-force value in a graph analogous to Fig. 6.

2) *Robot Thrust*: The flapping thrust (i.e., scalar value) is obtained by time-averaging over a flapping period, as in (9). Transient effects are filtered out by advancing the simulation for several periods and then considering the last ones. Relevant results are shown in Section V.

3) *Magnetic Resistant Torque and Corresponding Absorbed Power*: The MR torque T_m^{res} is computed by exploiting (10). A conservative estimate of the torque can be obtained by freezing the flap in its initial configuration. In fact, this imposes a reduced separation between facing magnets, therefore increasing the magnetic-interaction intensity. An example of the resistant torque trend over a period for such a conservative configuration is shown in Fig. 7. For corresponding experimental results, see Section V.

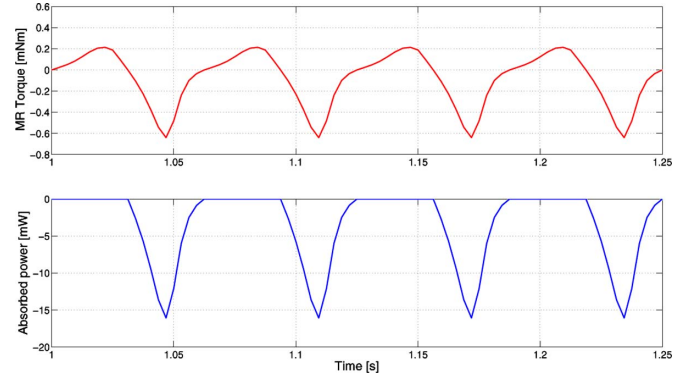


Fig. 8. Trend of MR torque and corresponding absorbed power over a flapping period. Parameters are as reported in Fig. 6.

The resistant-torque trend associated with the flap dynamics, i.e., accounting for the actual flap configuration over time, clearly differs from the one discussed above. A representative trend is shown in Fig. 8.

The proposed model also permits the power requirement associated with the MR torque to be easily estimated. Indeed, by recalling that the spindle angular velocity ω is assumed to be constant, the instantaneous power associated with the magnets rotation is $T_m^{\text{res}} \omega$. However, positive power contributions cannot be exploited by the considered system in the absence of a dedicated energy-storage mechanism. Hence, the absorbed power P_m^{abs} associated with magnets rotation reads

$$P_m^{\text{abs}} = T_m^{\text{res}} \cdot \omega \cdot H(-T_m^{\text{res}}) \quad (12)$$

where $H(\cdot)$ denotes the well-known Heaviside step function. A typical trend of P_m^{abs} over a flapping period is shown in the bottom half of Fig. 8. Besides predicting the peak value of P_m^{abs} , the proposed formulation also allows estimation of the average energy consumption per period due to the MR torque. Such a value can be directly used to define an energy budget of the proposed system, which accounts for other power requirements as well (e.g., system electronics, etc.).

4) *Dynamics Animation*: Once the differential problem (2) has been solved, it is easy to create effective animations during postprocessing, as an additional tool to support system development. Examples of animation frames are provided in the attached multimedia material, which shows a richer beam dynamics than the one in Fig. 6, due to a reduction in spindle frequency, i.e., 2 Hz instead of 4 Hz. In particular, a rebound occurs after the beam reaches the top displacement configuration, due to the increase in the passage time of the underneath rotating magnet: The mechanically pulled-back magnet on the flap encounters a magnetic field still significant enough to push it and produce a rebound.

IV. TECHNICAL IMPLEMENTATION

A swimming robot implementing the proposed principle is represented in Fig. 2. This four-flap swimmer was fabricated and assembled with the purpose of testing the novel strategy and validating the model. The robot prototype is shown in Fig. 9(a),

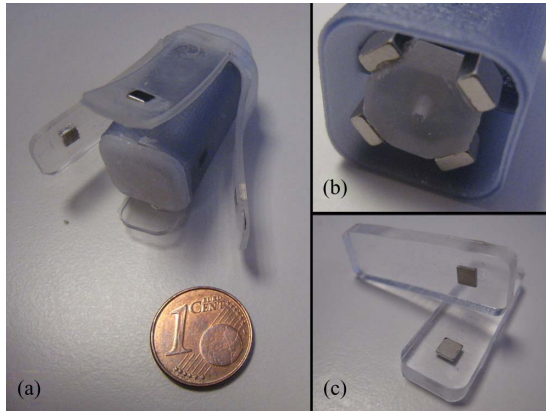


Fig. 9. (a) Assembled prototype. (b) Detail of the rotor. (c) Detail of the flaps.

while a zoomed view of the rotor and the flaps are provided in Fig. 9(b) and (c), respectively.

Magnetic forces are generated by eight N42 NdFeB magnets (K&J Magnetics, Jamison, PA), $3.18 \times 3.18 \times 1.59 \text{ mm}^3$ in size and weighing 0.12 g each. The maximum residual flux density of the NdFeB magnets is $B_{r \text{ max}} = 1.32 \text{ T}$. Four magnets are housed on the rotor, while the other four are placed on the internal surface of the flaps in a repulsive configuration. The current rotor is an octagonal cross-section module designed to support four equally spaced permanent magnets. It has a diameter of 8.5 mm and a thickness of 4 mm.

A dc brushless motor (SBL04-0829PG04-79, Namiki, Akita, Japan) was selected as the best tradeoff between size and stall torque (1.5 mN·m). The motor is 4 mm in diameter and 16.2 mm in length including the gearbox and weighs 1 g. A wireless microcontroller (CC2430, Texas Instruments, Dallas, TX), which is mounted on a custom-developed circular electronic board (9.6 mm in diameter, 2.3 mm in thickness, 0.28 g in weight, as described in [24]), was used to control the speed of the actuator by remotely taking advantage of back electromotive-force driving. This control unit potentially allows the acquisition of data from sensors and the control of additional actuators should they be embedded in future versions of the robot. A lithium ion polymer battery (LiPo) LP30 from Plantraco, having the highest energy density (200 Wh/kg) available for off-the-shelf components, was used to provide energy to all the active components. The LP30 is a 3.7 V LiPo cell with a nominal capacity of 30 mAh, a weight of 0.96 g, and very small size ($17 \times 10 \times 3 \text{ mm}^3$).

Considering the size of the aforementioned components, a rigid smooth squared-section shell was fabricated, which measured 35 mm in length and 15 mm in width. Although lacking hydrodynamic features, this shape was considered suitable since it may be easily assembled for the model-validation experiments. Rapid prototyping (InvisionSi2 by Inition, ThingLab, London, U.K.) was employed to manufacture both the shell and the rotor. The structural material is composed of urethane acrylate polymer (35%–45%) and triethylene glycol dimethacrylate ester (45%–55%).

Four elastic flaps are externally fixed to the robot body and depart from the top of the device. The flaps are manufactured in

polydimethylsiloxane (PDMS) material (Sylgard 184) and are $30 \times 10 \times 1.5 \text{ mm}^3$ in size. On one end, they are hinged to the robot body so that the active flap is 20-mm long, as in the model described in Section III. The opposite end of each flap embeds the NdFeB magnet. PDMS (whose Young's modulus is 1.76 MPa [25]) can be easily manufactured in different lengths, shapes, and thicknesses, thus allowing scalability of the flap.

Due to this modular architecture, the design and testing of many structural variations can be easily implemented. In particular, the robot can be scaled down in dimensions by, e.g., using a different actuator, reducing the flap size, and giving up wireless communication, thus reducing space required by electronics.

The overall weight of the robot was adjusted to achieve neutral buoyancy. The parameter δ_* , which is defined in Section III-B1, can be derived from the body width, flap thickness, rotor diameter, and magnet size, thus resulting in 3.2 mm.

A PC-based interface (which is developed in Labview 8.2, National Instruments) allows the user to interact with the robot by wireless communication. In particular, the user can set several working parameters, such as motor revolutions per minute, and can monitor the status of the robot, e.g., battery level and communication-signal strength.

V. EXPERIMENTAL RESULTS

A. Flap Dynamics

A preliminary experiment aimed at assessing flap dynamics in the developed model. In particular, the variation of the number of flap beats per minute with the increase in spindle-rotation frequency was measured in water and compared with model prediction.

A slow-motion video-capture system (i.e., HotShot 512 SC, NAC Image Technology, Inc.) was used to quantify the number of flap beats per minute performed by the robot prototype once immersed in a water tank. The robot was forced into a fixed position in order to enhance image acquisition. A single flap beat was counted every time the flap hit the case wall, after returning from the maximum-bending configuration. Spindle-rotation frequency was varied from 2 to 9 Hz, which is the maximum rotation speed for the adopted brushless motor.

The number of wall-flap contacts (i.e., beats per minute) during a period is expected to linearly increase with the rotating magnet frequency f as $60 N_m f$ up to a certain threshold value. Then, above this threshold, the considered number of contacts is expected to decrease due to the characteristic time of the flap mechanical response, with damping effects being systematically present (see also Section III-C). In particular, the model predicts such a transition between 7 and 8 Hz for the considered flap (see Fig. 10). Experimental results confirm the predicted linear trend for frequencies up to 5 Hz while also showing a plateau and consistent reduction starting from 6 Hz. The sharp transition predicted by the model is due to its intrinsic simplifications, which, however, do not prevent from assessing, with reasonable accuracy, the beating regime, above which, elasticity has an effect on flap dynamics. This kind of information is consistent with the modeling objectives. Moreover, an accurate description of flapping dynamics may only be pursued by taking

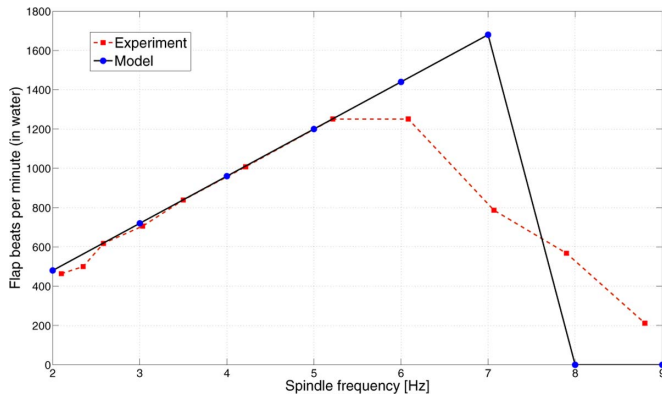


Fig. 10. Beats per minute of a flap immersed in water. Experimental values versus predicted ones. Parameters are as reported in Fig. 6, except for spindle-rotation frequency and $N_m = 4$.

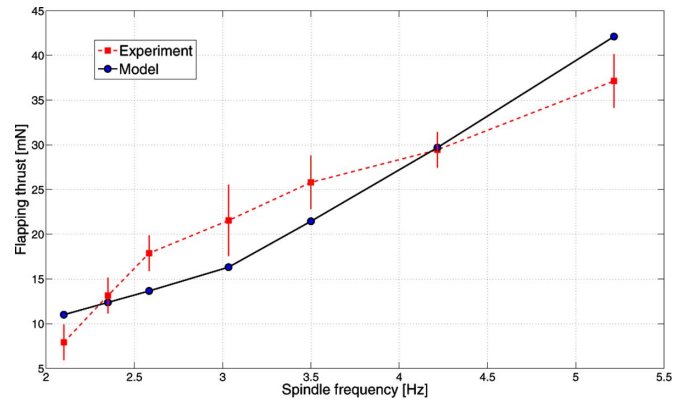


Fig. 12. Experimental thrust values versus predicted ones. Parameters are as reported in Fig. 6, except for spindle-rotation frequency.

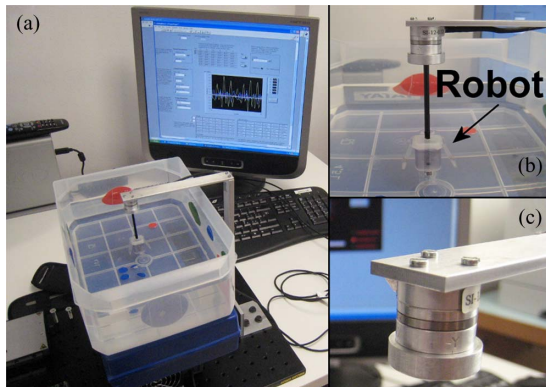


Fig. 11. (a) Test bench for thrust measurements. (b) Detail of the support. (c) Detail of the load cell.

into account complex 3-D effects such as hydrodynamic interactions between flaps, as well as flap twisting due to magnetic forces.

B. Robot Thrust

An experimental test bench, as represented in Fig. 11(a), was set up in order to measure the robot thrust and compare it with the model prediction. A commercial six-axis load cell [Nano17, ATI, Industrial Automation, Apex, NC; as represented in Fig. 11(c)], having a resolution of 0.78mN, was used for these experiments. The robot body was rigidly connected to the load cell, as shown in Fig. 11(b), and placed under water inside a tank. Spindle frequency was varied from about 2 to 5 Hz and the corresponding thrust values were measured.

Fig. 12 compares the predicted thrust, which results from (9), with the experimental values as the spindle frequency increases. The mean absolute error was 0.9 mN, while the average relative error was 2.5% over the full range of measurements, thus demonstrating good agreement of the model with experimental results.

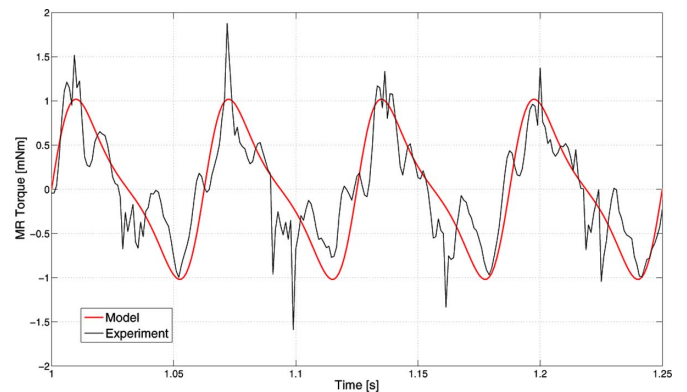


Fig. 13. Experimental trend of the MR torque versus the predicted one already presented in Fig. 7 (parameters cited therein).

C. Magnetic-Resistant Torque and Corresponding Absorbed Power

The same setup used to measure flapping thrust was adapted to quantify the MR torque, as defined in Section III-A8. In particular, the flaps were forced to be in contact with the case—as described in Section III-C3—and the case–flaps assembly was connected to the load cell, while the spindle with the rotating magnets was independently driven at different frequencies, i.e., from about 2 to 5 Hz.

A comparison between the experimental data and model prediction at $f = 4$ Hz is reported in Fig. 13. In this case also, the model agrees with experimental evidence, thus showing a mean relative error below 1% (with respect to the peak theoretical value) over the full range of measurements. High-frequency components in the experimental plot in Fig. 13 are essentially due to mechanical vibrations.

As already mentioned, the model allows prediction of the average energy consumption per period due to the MR torque. In particular, the model predicts a consumption of 1.16 mJ to drive the flap introduced in Section IV at 4 Hz. To assess this prediction, the current consumption of the motor was measured while driving the robot underwater, both with and without flaps. These measurements were repeated ten times for each configuration to obtain average values. The difference in

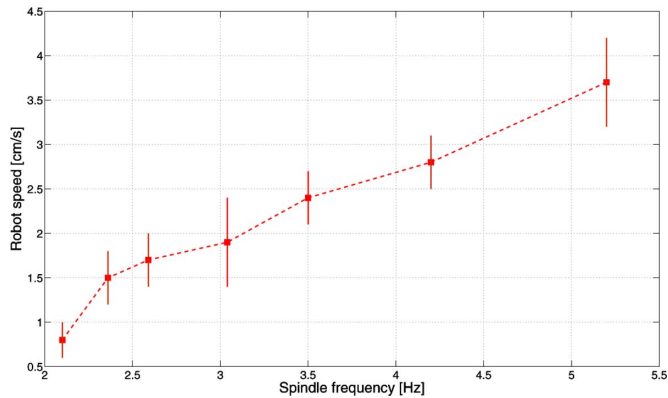


Fig. 14. Experimental trend of the robot swimming speed versus spindle frequency. Parameters are as reported in Fig. 6, except for spindle-rotation frequency.

current consumption between the two configurations was used in order to compute the power absorbed to drive the spindle against the magnetic torque, thus obtaining 4 mW. Considering a beating frequency of 4 Hz, this leads to an average consumption of 1 mJ per period, which is in agreement with the model prediction. The same level of matching between model and experiments was achieved at other frequencies.

D. Swimming Performance

The swimming performance was tested in a water-filled tank. Spindle frequency was varied from about 2 to 5 Hz, and the corresponding robot speed was measured. The results, which are averaged on five trials for each frequency, are reported in Fig. 14. The best performance in terms of speed was achieved at 5.2 Hz, where a peak of 3.7 cm/s (i.e., more than one body length per second) was achieved. In this configuration, the robot was able to swim in water for more than 20 min without recharging. Deviations from a straight trajectory observed during tests were mainly due to unavoidable asymmetries in the final assembly.

In order to evaluate the efficiency of the proposed mechanism, which is intended as ratio of output power to input power, and to compare it with other motion transmission solutions, we define

$$\eta = \frac{P_{\text{out}}}{P_{\text{in}}} = \frac{F_x^{\text{prop}} \cdot v_x}{T_m^{\text{res}} \cdot \omega} \quad (13)$$

where F_x^{prop} is the forward thrust averaged over the flapping period, v_x is the average forward speed, while T_m^{res} is the MR torque, and ω is the motor angular velocity. Given the experimental data, the average of the mechanism efficiency over the considered spindle-frequency range was 2.6%, thus reaching a peak of 4.9% at 5.2 Hz.

A movie of the robot while swimming is available as a multimedia attachment to this paper.

E. Model Prediction as Support to Robot Design

As already mentioned, the main purpose of the developed model is to straightforwardly provide cues to enhance robot performance. Therefore, once validated, we used the model to predict the relative variation of robot thrust in case a structural

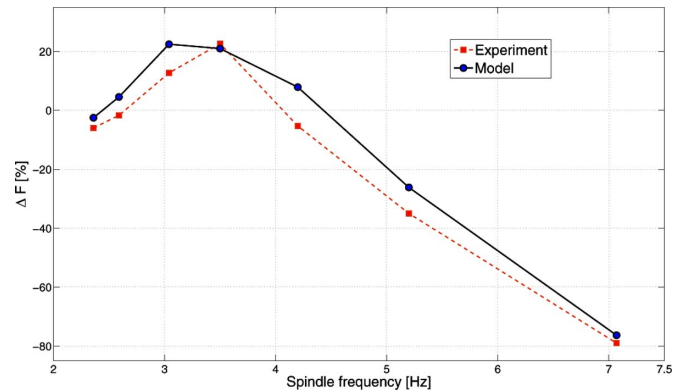


Fig. 15. Percentile thrust variation given by an active flap length increase of 25%. Parameters are as reported in Fig. 6, except for the flap length and the spindle-rotation frequency.

feature was changed. Among the many design and structural parameters described in Section II, we focused on flap length and spindle frequency. In particular, we increased the active flap length from 20 to 25 mm (i.e., a 25% length increase), and we varied the spindle frequency from about 2 to 7 Hz. The percentile increase of the robot thrust due to an active-flap-length increase of 25% is reported in Fig. 15 for both model prediction and experimental data. The average difference between model and prediction was 6.5% with a maximum value of 13.2%.

As reported in the graph, the model was able to predict around 20% increase in robot thrust for a specific spindle-frequency range and a dramatic decrease in performance as the spindle frequency increases. This can be explained by recalling the threshold frequency defined in Section V-A and the trend of flap beats per minute versus spindle frequency reported in Fig. 10. Considering that a longer flap has a slower mechanical response, the number of wall-flap contacts is expected to start decreasing at a smaller frequency, thus justifying the performance drop at high spindle frequencies. On the other hand, as long as the mechanical response of the flap is able to follow the spindle rotation, a longer flap results in a stronger thrust.

VI. CONCLUSION AND FUTURE DEVELOPMENTS

A novel actuation concept based on the interaction of permanent magnets was implemented in a miniature swimming robot. One of the main advantages of this mechanism is its flexibility, thereby allowing it to be applied to a wide range of applications. Modeling plays a crucial role in this scenario, since the physical and technical aspects involved need to be mastered not only in order to characterize system performance but in view of more extensive investigations, from system optimization to re-design, as well. In this spirit, we introduced a simple model capable of predicting the thrust achieved by flapping propulsion and of estimating the energy expenditure for actuation to potentially negotiate between the two. Due to a modular approach, additional entities to be predicted can be easily introduced in the proposed model, thus widening its potential impact on other kinds of robots. Once the model was calibrated by simple experiments, its outputs were compared with the actual robot

performance within the operational spindle-frequency range, i.e., from 2 to 5 Hz. Finally, the model was used as a design tool to investigate the effect of a 25% increase in active flap length at different spindle frequencies, i.e., from about 2 to 7 Hz.

As already mentioned, the main aim of this study was not to address a single application for underwater robots, thus focusing on swimming speed and efficiency but, rather, to elucidate the challenges involved both in designing a novel actuation mechanism and in developing a first-order model to predict mechanism behavior. Indeed, enhanced swimming performances can be obtained by tailoring some of the features described in Section II toward specific applications. Furthermore, the current model is unable to predict robot swimming speed. More refined fluidic modeling would allow the main physical mechanisms of thrust formation during flapping to be investigated, thus providing additional support to the design phase. A first step in that direction would be to look into the effect of neighboring flaps on the robot thrust.

Since the current version of the swimmer is only able to move forward, due to the symmetrical design, its elective application could be in random-swimming swarm robotics. Once provided with a chemical sensor, a swarm of these miniature robots could be deployed in a liquid environment to monitor water pollution.

As previously mentioned, the actuation principle and the related model can be easily extended to terrestrial locomotion, while the model itself may be used to approach general problems regarding the interaction between elastic and magnetic structures in other fields of robotics.

ACKNOWLEDGMENT

The authors would like to thank N. Funaro, C. Filippeschi, G. Favati, and A. Melani, as well as Dr. E. Susilo, Dr. V. Pensabene, and G. Bonsignori for their invaluable technical support.

REFERENCES

- [1] P. Valdastri, P. Corradi, A. Menciassi, T. Schmickl, K. Crailsheim, J. Seyfried, and P. Dario, "Micromanipulation, communication and swarm intelligence issues in a swarm microrobotic platform," *Robot. Auton. Syst.*, vol. 54, no. 10, pp. 789–804, 2006.
- [2] S. Guo, Q. Pan, and M. B. Khamesee, "Development of a novel type of microrobot for biomedical application," *Microsyst. Technol.*, vol. 14, no. 3, pp. 307–314, 2008.
- [3] S. Martel, O. Felfoul, J. B. Mathieu, A. Chanu, S. Tamaz, M. Mohammadi, M. Mankiewicz, and N. Tabatabaei, "MRI-based medical nanorobotic platform for the control of magnetic nanoparticles and flagellated bacteria for target interventions in human capillaries," *Int. J. Robot. Res.*, vol. 28, no. 9, pp. 1169–1182, 2009.
- [4] J. J. Abbott, M. C. Lagomarsino, L. Zhang, L. Dong, and B. J. Nelson, "How should microrobots swim?," *Int. J. Robot. Res.*, vol. 28, no. 11/12, pp. 1434–1447, 2009.
- [5] J. J. Abbott, Z. Nagy, F. Beyeler, and B. J. Nelson, "Robotics in the small, part I: Microbotics," *IEEE Robot. Autom. Mag.*, vol. 14, no. 2, pp. 92–103, Jun. 2007.
- [6] B. Behkam and M. Sitti, "Modeling and testing of a biomimetic flagellar propulsion method for microscale biomedical swimming robots," in *Proc. IEEE/ASME Int. Conf. Adv. Intell. Mechatron.*, 2005, pp. 37–42.
- [7] G. Kosa, M. Shoham, and M. Zaaroor, "Propulsion method for swimming microrobots," *IEEE Trans. Robot.*, vol. 23, no. 1, pp. 137–150, Feb. 2007.
- [8] B. Kim, D.-H. Kim, J. Jung, and J.-O. Park, "A biomimetic undulatory tadpole robot using ionic polymer metal composite actuators," *Smart Mater. Struct.*, vol. 14, no. 6, pp. 1579–1585, 2005.
- [9] Z. G. Zhang, N. Yamashita, M. Gondo, A. Yamamoto, and T. Higuchi, "Electrostatically actuated robotic fish: Design and control for high-mobility open-loop swimming," *IEEE Trans. Robot.*, vol. 24, no. 1, pp. 118–129, Feb. 2008.
- [10] P. Kodati, J. Hinkle, A. Winn, and X. Deng, "Microautonomous robotic ostraciiform (MARCO): Hydrodynamics, design, and fabrication," *IEEE Trans. Robot.*, vol. 24, no. 1, pp. 105–117, Feb. 2008.
- [11] X. Tan, D. Kim, N. Usher, D. Laboy, J. Jackson, A. Kapetanovic, J. Rapai, B. Sabadus, and X. Zhou, "An autonomous robotic fish for mobile sensing," in *Proc. IEEE/RSJ Int. Conf. Intell. Robot. Syst.*, Oct. 9–15, 2006, pp. 5424–5429.
- [12] G. Tortora, P. Valdastri, E. Susilo, A. Menciassi, P. Dario, F. Rieber, and M. O. Schurr, "Propeller-based wireless device for active capsular endoscopy in the gastric district," *Minim. Invasive Ther. Allied Technol.*, vol. 18, pp. 280–290, Jan. 2009.
- [13] C. Pawashe, S. Floyd, and M. Sitti, "Modeling and experimental characterization of an untethered magnetic micro-robot," *Int. J. Robot. Res.*, vol. 28, no. 8, pp. 1077–1094, 2009.
- [14] K. B. Yesin, K. Vollmers, and B. J. Nelson, "Modeling and control of untethered biomicrobots in a fluidic environment using electromagnetic fields," *Int. J. Robot. Res.*, vol. 25, no. 5/6, pp. 527–536, 2006.
- [15] Z. Chen, S. Shataru, and X. Tan, "Modeling of biomimetic robotic fish propelled by an ionic polymer–metal composite caudal fin," *IEEE/ASME Trans. Mechatron.*, vol. 15, no. 3, pp. 448–459, Jun. 2010.
- [16] K. A. Morgansen, B. I. Triplett, and D. J. Klein, "Geometric methods for modeling and control of free-swimming fin-actuated underwater vehicles," *IEEE Trans. Robot.*, vol. 23, no. 6, pp. 1184–1199, Dec. 2007.
- [17] W. Liu, A. Menciassi, S. Scapellato, P. Dario, and Y. Chen, "A biomimetic sensor for a crawling minirobot," *Robot. Auton. Syst.*, vol. 54, no. 7, pp. 513–528, 2006.
- [18] L. Landau and E. Lifshitz, *Theory of Elasticity*. New York: Pergamon, 1970.
- [19] A. Erturk and D. Inman, "Issues in mathematical modeling of piezoelectric energy harvesters," *Smart Mater. Struct.*, vol. 17, pp. 065016–065029, 2008.
- [20] J. Dormand and P. Prince, "A family of embedded Runge–Kutta formulae," *J. Comp. Appl. Math.*, vol. 6, pp. 19–26, 1980.
- [21] R. P. Feynman, R. B. Leighton, and M. Sands, *The Feynman Lectures on Physics*. Reading, MA: Addison-Wesley, 1964.
- [22] J. Sparenberg, "Survey of the mathematical theory of fish locomotion," *J. Eng. Math.*, vol. 44, pp. 395–448, 2002.
- [23] W. C. Sandberg and R. Ramamurti, "3-D unsteady computations of flapping force production in swimming fish, flying insects, and unmanned vehicles," *Bio-Mechanisms of Swimming and Flying*, N. Kato and S. Kamimura, Eds., Tokyo, Japan: Springer, 2008, ch. 17, pp. 205–217.
- [24] E. Susilo, P. Valdastri, A. Menciassi, and P. Dario, "A miniaturized wireless control platform for robotic capsular endoscopy using advanced pseudokernel approach," *Sensors Actuators A: Phys.*, vol. 156, no. 1, pp. 49–58, 2009.
- [25] F. Schneider, J. Draheim, R. Kamberger, and U. Wallrabe, "Process and material properties of polydimethylsiloxane (PDMS) for optical MEMS," *Sensors Actuators A: Phys.*, vol. 151, no. 2, pp. 95–99, 2009.



Pietro Valdastri (M'05) received the Master's degree (Hons.) in electronic engineering from the University of Pisa, Pisa, Italy, in 2002 and the Ph.D. degree in bioengineering from the Scuola Superiore Sant'Anna, Pisa, in 2006.

He is currently an Assistant Professor of biomedical robotics with the Scuola Superiore Sant'Anna, where he is engaged in research on implantable robotic systems and active capsule endoscopy.



Edoardo Sinibaldi received the Master's degree (*magna cum laude*) in aerospace engineering from the University of Pisa, Pisa, Italy, in 2002 and the Ph.D. degree (*magna cum laude*) in mathematics for technology and industry from the Scuola Normale Superiore, Pisa, in 2006.

Since November 2009, he has been a Senior Postdoctoral Researcher with the Italian Institute of Technology, Scuola Superiore Sant'Anna Center, Pontedera, Italy. His current research interests include theoretical modeling and numerical simulation of fluids

and microbiorobotic systems.



Sebastiano Caccavaro received the Master's degree in mechanical engineering from the University of Calabria, Cosenza, Italy, in 2008. He is currently working toward the Ph.D. degree in microsystems engineering with the BioRobotics Institute, Scuola Superiore Sant'Anna, Pisa, Italy.

His current research interests include biomedical robotics, minimally invasive surgery, and computer-assisted surgery.



Arianna Menciassi (M'00) received the Master's degree (Hons.) in physics from the University of Pisa, Pisa, Italy, in 1995 and the Ph.D. degree from the Scuola Superiore Sant'Anna (SSSA), Pisa, in 1999.

She is currently an Associate Professor of biomedical robotics with SSSA. Her current research interests include biomedical micro- and nanorobotics for the development of innovative devices for surgery, therapy, and diagnostics.



Giuseppe Tortora (S'09) was born in Isernia, Italy, in 1983. He received the M.S. degree in bioengineering from the University of Pisa, Pisa, Italy, in April 2008. He is currently working toward the Ph.D. degree in biorobotics with the Scuola Superiore Sant'Anna, Pisa.

In April 2007, he joined the BioRobotics Institute, Scuola Superiore Sant'Anna, where he was engaged in capsular endoscopy. His current research interests include biorobotics, endoscopy, and minimally invasive robotic surgery.



Paolo Dario (F'02) received the Master's degree in mechanical engineering from the University of Pisa, Pisa, Italy, in 1977.

He is currently a Professor of biomedical robotics with the Scuola Superiore Sant'Anna, Pisa, where he supervises a team of about 150 young researchers. His current research interests include biorobotics, including mechatronic and robotic systems for rehabilitation, prosthetics, surgery, and microendoscopy.

Prof. Dario is a recipient of the Joseph Engelberger Award as a Pioneer of Biomedical Robotics.